The International Journal of Advanced Manufacturing Technology (2023) 128:2319–2331
https://doi.org/10.1007/s00170-023-12093-7

ORIGINAL ARTICLE

Modeling and simulation of material removal characteristics in magnetorheological shear thickening polishing

Zhen Ma[1] · Yebing Tian[1,2] · Cheng Qian[1] · Shadab Ahmad[1,3] · Zenghua Fan[1,2] · Zhiguang Sun[1]

Received: 23 December 2022 / Accepted: 31 July 2023 / Published online: 5 August 2023

Abstract
Magnetorheological shear thickening polishing (MRSTP) was experimentally demonstrated to achieve nano-level surface quality in previous studies. The aim of work is to further investigate numerical simulation and material removal characteristics during the MRSTP process. The apparatus of magnetic field generation was designed and developed. The model of magnetic field distribution was imported to computational fluid dynamics (CFD) module to generate desired polishing environment. Polishing stress behaviors were analyzed based on various polishing parameters through the CFD simulation results. It was found that the pressure on the workpiece surface decreased with the increase of the rotational speed of the workpiece while it increased with the increase of the flow velocity of the MRSTP media. A continuous increment in shear stress on the workpiece surface was observed with the increase of the rotation speed of the workpiece and the flow velocity of the MRSTP media. Based on the characteristics of polishing pressure, material removal rate (MRR) model of MRSTP process was established. A serial of MRSTP experiments were conducted on aluminum 6061. Surface roughness (Sa) of 79.0 nm was obtained, which was improved over 77%. The simulated model and MRR model were experimentally validated. The average error between theoretical and experimental results was 4.1%. It can provide a useful guidance for the novel MRSTP process.

Keywords Magnetorheological shear thickening polishing · Numerical simulation · Force characteristics · Material removal model

1 Introduction

Magnetic field assisted polishing (MFAP) methods have become one of research hotspots due to their flexibility, self-sharpening and self-adaptability for the recent years. MFAP methods are widely employed for polishing various hard-to-process materials, such as silicon, sapphire, glass, ceramic, superalloy. Barman et al. [1] investigated the influence of magnetorheological (MR) polishing fluids with different compositions on polishing performance. Two different MR fluids were utilized to polish the bio-titanium alloy to obtain hydrophilic and hydrophobic surfaces, respectively. Zhai et al. [2] proposed ultrasound assisted magnetorheological polishing (UAMP) on sapphire and established a material removal rate (MRR) model of UAMP based on the Preston equation. The feasibility of this model was experimentally verified. Luo et al. [3] conducted polishing experiments on zirconia ceramics using MRP method. Surface roughness R_a of zirconia ceramics decreased to 0.702 nm from initial 71.976 nm using diamond abrasive particles. The maximum material removal rate of 1 mg/min was attained. Yamaguchi et al. [4] employed magnetic abrasive finishing (MAF) method to improve the tool life of uncoated WC/Co cutting tool. It was concluded that the cutting tool life was improved by 150%. Li et al. [5] performed a hybrid post-processing of MAF and heat treatment (HT) on the surface of 3D-printed Inconel 718 alloy. The surface roughness Ra of the workpiece decreased to 0.15 μm from initial 2.7 μm. The hybrid post-treatment of MAF and HT demonstrated that the mechanical properties such as yield strength and elongation of the Inconel 718 alloy manufactured in additive form

✉ Yebing Tian
tianyb@sdut.edu.cn; tyb79@sina.com

1 School of Mechanical Engineering, Shandong University of Technology, 266 Xincun West Road, Zibo, Shandong 255049, People's Republic of China

2 Institute for Advanced Manufacturing, Shandong University of Technology, Zibo 255049, People's Republic of China

3 Centre for Advanced Production and Industrial Engineering Research, Delhi Technological University, Delhi 110042, India

were significantly improved. Umehara et al. [6] designed and fabricated a novel magnetic floating polishing platform for large-size and large-volume silicon nitride (Si_3N_4) balls. The polishing process was divided into three stages i.e., roughing stage, intermediate stage and finishing stage. The surface roughness Ra of the polished silicon nitride (Si_3N_4) balls decreased to 6.70 nm from initial 937.14 nm.

For the MFAP method, a lot of numerical simulations were employed to understand the effects of processing parameters on the polishing performance before the experiments were conducted. This facilitated the simplification of tests and efficiency improvement. Kumar et al. [7] investigated the mechanism of magnetorheological polishing on miniature tooth contours where the forces on the surface of the micro-gear were simulated using COMSOL software. A surface roughness model of polished micro-gear was established using simulation results. Wang et al. [8] proposed a new magnetic field assisted mass polishing technology for efficient polishing of multiple free-form parts simultaneously. The effect of magnetic field on the material removal characteristics was analyzed by the finite element method. The factors affecting surface generation were investigated by polishing experiments. The results showed that magnetic field assisted mass polishing could effectively polish multiple free-form parts with nano-level surface finish. Liu et al. [9] simulated the three-dimensional profile of the polishing points during magnetorheological polishing. A material removal rate (MRR) model considering pressure and shear stress was developed using the simulation results, which was verified for accuracy. Sharma [10] simulated the magnetic field strength of the newly designed magnetorheological polishing equipment. A mathematical model of the relationship between surface roughness and magnetic field strength was established. The results showed that the surface roughness decreased with the increase of magnetic field strength. Grover et al. [11] designed a magnetorheological polishing equipment for polishing cylindrical inner surfaces using radially curved permanent magnets. Simulation of the magnetic field strength of this radially curved permanent magnet was conducted. A mathematical model for predicting surface roughness was developed based on the results of the simulation. After validation, the maximum error of the model was 8.06%. Guo et al. [12] designed a novel magnetorheological polishing equipment with Halbach array for quartz specimens. The magnetic field strength of Halbach array was simulated to verify its large area and high strength. The surface roughness of the quartz specimen eventually improved up to 0.544 nm after polishing.

An accurate material removal model is of benefit to provide theoretical guidance and reveal the polishing mechanism. Great efforts have been made to establish the predictive material removal model for the MFAP. Zhai et al. [2] developed a material removal model for magnetorheological polishing where the coupling effect of magnetic and vibrational fields was considered. It was verified that the relative error between the theoretical and experimental results was less than 20%. Chen et al. [13] established a two-dimensional material removal model for magnetorheological polishing based on hydrodynamic theory and the Preston equation. The rationality of the material removal model was verified by comparing the experimental results with the simulation results. The error between the model and the experimental results was 9.8%. Ming et al. [14] established a material removal model for a non-Newtonian fluid polishing method based on weak magnetorheological strengthening thickening effects. The model was developed using non-Newtonian fluid kinematics. The average error between the model and experimental results was 4.45%. Li et al. [15] established a material removal model for the magnetic abrasive finishing method using fluid abrasives in which the effect of magnetic fields on material removal was considered. This model agrees to the experimental results with an average error of 4.51%.

In our previous studies, magnetorheological shear thickening polishing (MRSTP) was proposed as a novel magnetic field assisted polishing process which combined the magnetorheological effect with the shear thickening effect together [16–19]. As one of loosed abrasive polishing methods, MRSTP possesses excellent adaptability and processing efficiency. It has a magnetorheological effect that enables the rapid formation of magnetically enhanced particle clusters in the polishing media under the excitation of a magnetic field [16]. These clusters exert much stronger holding force on the abrasive particles, which makes the polishing process more efficient than the traditional MFAP. Additionally, MRSTP has a shear thickening effect during polishing, which results in larger shear stress on the workpiece surface than the conventional MRF. Due to its high adaptability and efficiency, MRSTP has been used to polish various difficult-to-machine materials [16–19]. MRSTP media was prepared by mixing a certain proportion of polyethylene glycol (PEG 200), SiO_2, abrasives, carbonyl iron powder (CIP) and chemical additives [16]. Simulation of the magnetic field strength of the magnetic field generation device was performed to verify the rationality of the structure [17]. The magnetic field generator and the modified magnetic abrasive were used to polish the titanium alloy Ti-6Al-4 V. Surface roughness of workpiece reduced from 1.17 μm to 54 nm. Also, in a case MRSTP media were specially developed for titanium alloy under the action of a four-pole rotating magnetic field [18]. The surface roughness of titanium alloy Ti-6Al-4 V was reduced from 169 to 61 nm and the effectiveness of this polishing media was verified. A new magnetic field generation device was designed which was capable of generating alternating magnetic fields for the additive manufacturing of 361L rectangular micro-fabricated structures[19]. Material removal rate models were developed and processing experiments were conducted. The results showed that the top and bottom of the rectangular microstructure were uniformly removed from the material. The feasibility of machining additively manufactured workpieces with MRSTP media was verified.

Nevertheless, recent studies on MRSTP were focused on processing experiments and simulation of magnetic fields. The coupling simulation of magnetic and flow fields in the MRSTP process with CFD methods was not explored. Therefore, in this work, CFD simulations of the designed MRSTP apparatus were carried out using Maxwell and Fluent modules in ANSYS software. It aimed to investigate the pattern of influence of polishing parameters on the polishing force applied to the workpiece surface. A mathematical model between MRR and polishing parameters was developed using the output of the normal forces from the CFD simulation results. The accuracy of the MRR model and the validity of the simulation results were verified by experiments.

2 Principles

Figure 1 shows the principle of MRSTP. MRSTP media are distributed inside polishing bowl which is fixed on the rotary table of either CNC machine or industrial robot. The magnetic field generation device is mounted below the polishing bowl. The workpiece is clamped onto the spindle bottom of either CNC machine or industrial robot. Under the action of the magnetic field, the MRSTP media form magnetic-force-reinforced flexible abrasive clusters. As the magnetic field has adsorption effect on the CIP, the shear rate of the MRSTP media will decrease when they flow through the magnetic field. This is macroscopically expressed as an increase in the apparent viscosity of the MRSTP media. The MRSTP media move in a circular motion driven by the rotary polishing bowl. The CIP and abrasive grains in the magnetic-force-reinforced flexible abrasive clusters are constantly renewed and pass through the immersed workpiece. The relative velocity between the MRSTP media and the workpiece is easily controlled by the spindle and the rotary table of either CNC machine or industrial robot.

3 Design of magnetic field generation device

Figure 2 shows the three-dimensional model and two-dimensional model of the magnetic field generation device. The device comprises of two magnetic pole mounts and twelve magnetic poles. The two pole mounts were made of Steel 45 with twelve holes (i.e., each mount had six poles) for holding the magnetic poles. The six poles were divided into three sets i.e., the top set, the middle set and the bottom set. The middle set were designed at an angle of 120° to the bottom sets. The material of all twelve poles was chosen as N38. The distribution of the magnetic field was simulated using Maxwell software. The materials defined in the model for the magnetic field generation device were same as those used in the actual polishing process. Three lines were planned for the measurement of magnetic field strength as shown in Fig. 2. The magnetic field intensity along the design path was measured using a Gauss meter (Model: GM 500).

Figure 3 shows the results of the magnetic field simulation. It can be seen that the magnetic force lines uniformly distributed in the polished area while magnetic field intensity were still strong around the workpiece. The maximum magnetic field strengths of 525.7 mT and 527.1 mT were obtained at the starting points of lines 1 and 3, respectively. Along line 1 and line 3, the magnetic field strength decreased with the increase of the distance. A maximum magnetic field strength of 183.3 mT was obtained at 3 mm away from the starting point of the line 2. As shown in Fig. 3 (a), since the magnetic force lines at the starting point of line 2 was not close to the magnetic field generating device, the magnetic field strength along line 2 firstly increased and then decreased with the distance increasing from the starting point.

Figure 4 shows the comparisons of magnetic field intensity between the simulation and experimental results. It

Fig. 1 Principle of the MRSTP

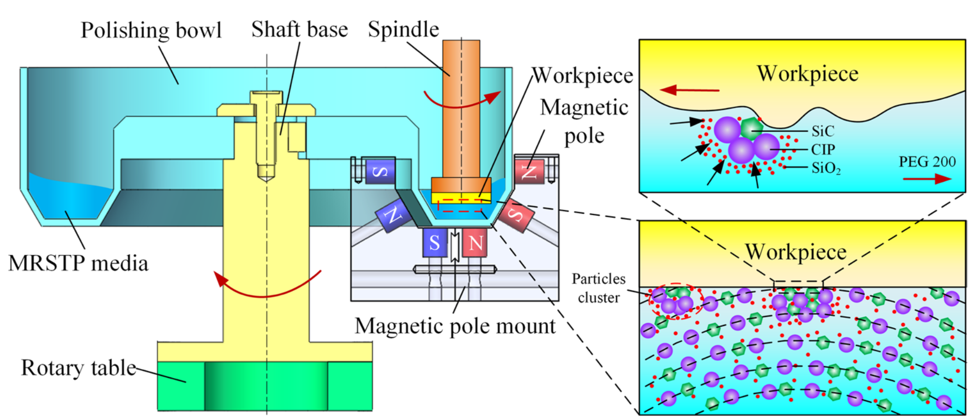

can be seen that the measured magnetic field strengths are consistent with the simulation values. The measured values at the starting point of the line 1 and line 3 were 315.4 mT and 367.0 mT, respectively. The measured value was 125.3 mT at 3 mm away from the starting point of the line 2. The validity of the simulation was verified.

4 Numerical simulation of flow field

4.1 Computational fluid dynamics methods

The flow field of the MRSTP process was numerically simulated using Ansys Fluent. Mixture models including STFs, CIP, SiC

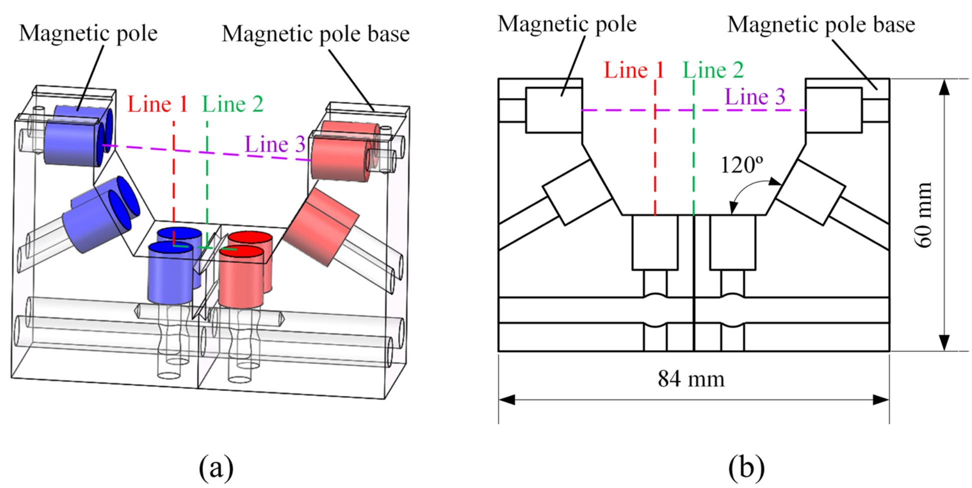

Fig. 2 Model of magnetic field generating device. (**a**) 3D model, (**b**) 2D model

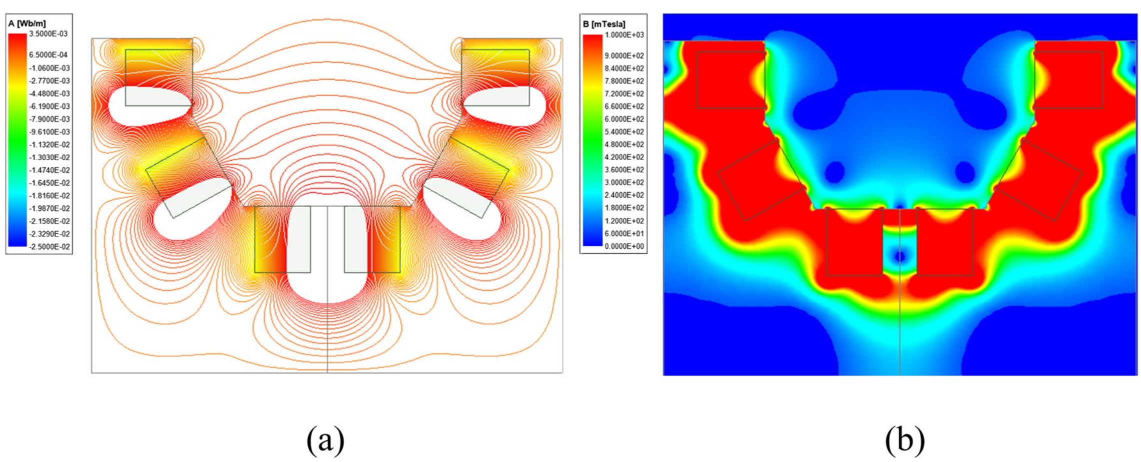

Fig. 3 Maxwell simulation results. (**a**) Distribution of magnetic force lines, (**b**) Distribution of magnetic field intensity

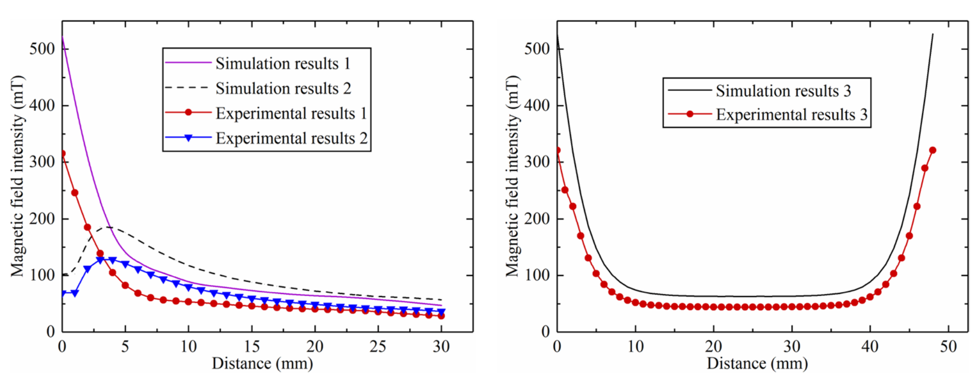

Fig. 4 Comparisons of magnetic field intensity between simulations and experiments

and other multiphase blends were used. The output from Maxwell was coupled using the MHD module in Fluent to simulate the magnetic field environment in the flow field. The following assumptions were made during this numerical simulation: (i) The workpiece was an ideal rigid material. (ii) The processing environment temperature was controlled at 25℃. In the MRSTP process, it was assumed that the fluid was incompressible and operated in a constant temperature environment. Hence, the continuity and momentum equations for incompressible viscous fluids were used to describe the motion state of the MRSTP media [20]:

$$\frac{\partial u}{\partial x} + \frac{\partial v}{\partial y} + \frac{\partial w}{\partial z} = 0 \tag{1}$$

$$\begin{cases} \frac{\partial u}{\partial t} + (V \cdot \nabla)u = f_x - \frac{1}{\rho}\frac{\partial p}{\partial x} + \frac{1}{\rho}\left(\frac{\partial \sigma_{xx}}{\partial x} + \frac{\partial \tau_{yx}}{\partial y} + \frac{\partial \tau_{zx}}{\partial z}\right) \\ \frac{\partial v}{\partial t} + (V \cdot \nabla)v = f_y - \frac{1}{\rho}\frac{\partial p}{\partial y} + \frac{1}{\rho}\left(\frac{\partial \sigma_{yy}}{\partial y} + \frac{\partial \tau_{zy}}{\partial z} + \frac{\partial \tau_{xy}}{\partial x}\right) \\ \frac{\partial w}{\partial t} + (V \cdot \nabla)w = f_z - \frac{1}{\rho}\frac{\partial p}{\partial z} + \frac{1}{\rho}\left(\frac{\partial \sigma_{zz}}{\partial z} + \frac{\partial \tau_{xz}}{\partial x} + \frac{\partial \tau_{yz}}{\partial y}\right) \end{cases} \tag{2}$$

where V is the velocity of the fluid. u, v, and w are the components of the fluid velocity in the x, y, and z directions. ρ is the density of the fluid. p is the pressure of the fluid. f is the mass force acting on the fluid. σ and τ are stress components.

The magnetic force on the fluid in the MHD model can be calculated by the following equation:

$$\begin{cases} \vec{f}_{m,x} = \mu_0\left(\vec{M}_x\frac{\partial H_x}{\partial x} + \vec{M}_y\frac{\partial H_x}{\partial y} + \vec{M}_z\frac{\partial H_x}{\partial z}\right) \\ \vec{f}_{m,y} = \mu_0\left(\vec{M}_x\frac{\partial H_y}{\partial x} + \vec{M}_y\frac{\partial H_y}{\partial y} + \vec{M}_z\frac{\partial H_y}{\partial z}\right) \\ \vec{f}_{m,z} = \mu_0\left(\vec{M}_x\frac{\partial H_z}{\partial x} + \vec{M}_y\frac{\partial H_z}{\partial y} + \vec{M}_z\frac{\partial H_z}{\partial z}\right) \end{cases} \tag{3}$$

where μ_0 is the vacuum permeability. M_x, M_y and M_z are the components of the magnetization intensity in the x, y, and z directions. H_x, H_y and H_z are the component of the magnetic field intensity in the x, y, and z directions.

The motion pattern of the fluid can be obtained from the calculation formula of Reynolds number Re:

$$Re = \frac{\rho \bullet v \bullet d_{re}}{\mu} \tag{4}$$

where ρ is the density of the fluid, v is the velocity of the fluid, μ is the dynamic viscosity of the fluid, d_{re} is the characteristic length of the fluid. The flow state of the MRSTP media was determined to be laminar based on the experimental parameters calculated as Re < 2320. The SIMPLE algorithm was used to solve the coupled velocity–pressure problem. Since the diffusion effect in the MRSTP media flow process could be neglected, it was a pure convection problem and the discrete format for establishing the discrete equations adopted the second order windward format.

4.2 Geometric model for numerical simulation

Figure 5 shows the geometric model for the numerical simulation in the software of Ansys Fluent. In order to reduce the computational effort and facilitate the computational convergence, the circular polishing bowl of MRSTP was designed as a linear polishing trough. This linear polishing trough had a velocity inlet on one side and a pressure outlet on the other side. The wall of the polishing trough was defined as non-slip wall surface. The wall of the workpiece was set up as rotational wall surface. As the top surface of the polishing trough was MRSTP medium, it was defined as symmetric boundary. In order to improve the computational accuracy, the polished trough was unstructured meshed. The grid size was chosen as 1 mm while the grid was encrypted near the workpiece with size of 0.5 mm. The magnetic field simulation results from the Sect. 3 were further processed and loaded into the software of Ansys Fluent. The loading results are shown in Fig. 5 (c). There was not any distortion observed in the magnetic field and the loading results were accurate. Two lines, AB and CD, were set up on the workpiece surface as the output locations of pressure and shear force in the simulation results, respectively.

4.3 Input parameters for numerical simulation

The simulation input parameters are listed in Table 1. The effects of with the rotational speed of workpiece and the flow velocity of the MRSTP media on the normal pressure and shear force on the workpiece surface were investigated. The maximum magnetic field strength was obtained along line 2 at 3 mm from the starting point as shown in Fig. 4 (a). Considering the existence of excitation gap and the thickness of polishing bowl in the actual processing, the gap between the workpiece and the bottom of the polishing trough was set up as 1 mm.

The rheological profiles of the STFs were measured in order to give shear thickening effect to the MRSTP media during the numerical simulation [16]. When the shear rate is less than the critical shear rate, STFs show shear thinning action. When the shear rate is between the critical shear rate and the maximum shear rate, the STFs show shear thickening action [21–23]. When the shear rate is greater than the maximum shear rate, the STFs show a shear thinning action. The viscosity of the STFs was defined in FLUENT using this rheological curve via programming with C language (Fig. 6).

4.4 Analysis of simulation results

4.4.1 Variation of normal pressure

In the Preston equation, the material removal rate during polishing is associated to the normal pressure on the surface of the workpiece and the velocity of the relative motion

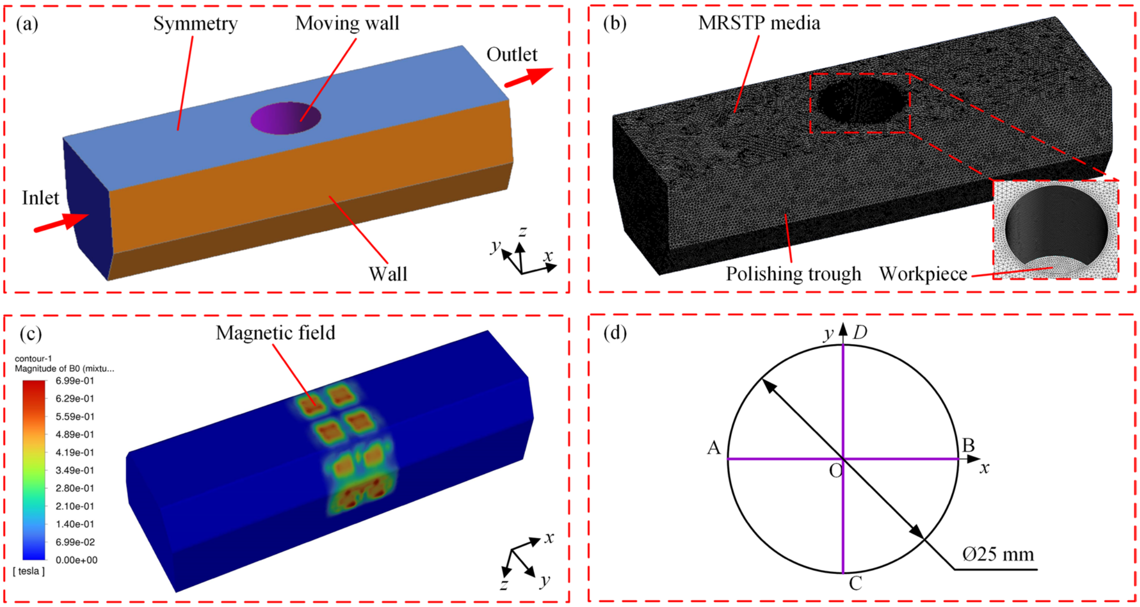

Fig. 5 Simulation models. (**a**) 3D model of a linear polishing trough, (**b**) Grid division, (**c**) Results of magnetic field loading, (**d**) Position of the force measurement on the surface of the workpiece

Table 1 Input parameters used for simulation study

Items	Values
Workpiece rotational speed (rpm)	1000, 1500, 2000
Flow velocity of MRSTP media (m/s)	0.8, 1.2, 1.6,
Working gap (mm)	1
Density of STFs (kg/m^3)	1796.64
Volume fraction of CIP	5.1%
Volume fraction of SiC	4.2%
Workpiece material	6061

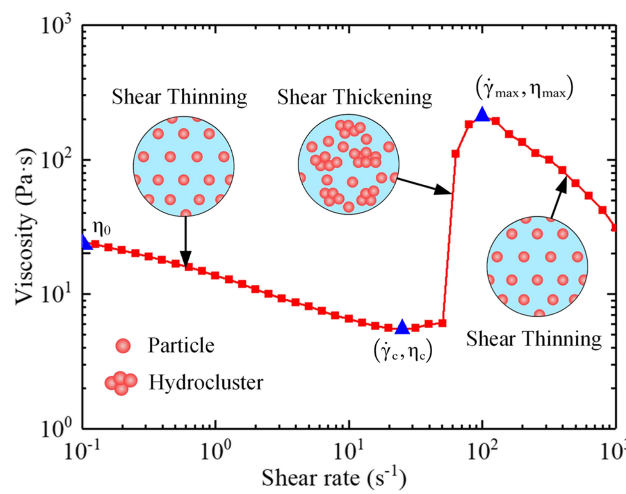

Fig. 6 Variation of STFs viscosity with shear rate

between the workpiece and the polishing fluid [24]. Therefore, it is essential to investigate the normal pressure distribution and variation on the workpiece surface through numerical simulation of the flow field.

Figure 7 shows the variation of normal pressure distribution versus different workpiece rotational speeds with the increase of working distance at the MRSTP media velocity of 0.8 m/s. It can be seen that the normal pressure distribution on the surface of the workpiece decreased along the *x*-direction and almost unchanged along the *y*-direction. This main reason was because the MRSTP media flowed along the *x*-direction. When the MRSTP media flowed under the workpiece, the height of the flow channel suddenly became narrow that made the MRSTP media to gather over one side of the workpiece and generated great pressure on the workpiece surface. Meanwhile, due to the high kinetic energy of the MRSTP media, the strong impact produced a large normal pressure on the surface of the workpiece when the media got to touch the workpiece surface. As the kinetic energy of the MRSTP media was gradually consumed with the flow of MRSTP media over the workpiece surface, the normal pressure on the workpiece surface slightly decreased.

The normal pressure on the workpiece surface gradually decreased as the workpiece rotational speeds increased from 1000 to 2000 rpm. As the rotation speeds of the workpiece increase, the MRSTP media underneath the workpiece will be driven by the workpiece to increase the flow rate. In this case, the normal pressure on the surface of the workpiece decreased, which was in accordance with the description of Bernoulli's principle.

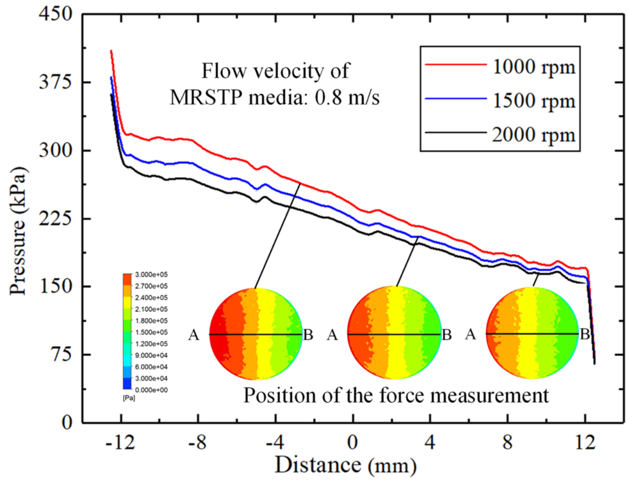

Fig. 7 Variation of normal pressure distribution versus workpiece rotational speed

Figure 8 shows the variation of normal pressure distribution versus the MRSTP media flow velocity of 0.8 m/s, 1.2 m/s and 1.6 m/s with the increase of working distance at the workpiece rotational speed of 2000 rpm. With the increase of flow velocity of MRSTP media, the normal pressure on the surface of the workpiece gradually increased as the kinetic energy became large.

4.4.2 Variation of shear stress

Shear stress is mainly caused by the fluid viscosity when the fluid media flow through the workpiece contact surface. In the ultraprecision polishing with non-newton fluid, material removal from the workpiece surface is not only related to the normal pressure but also the shear stress on the workpiece. Therefore, it is also important to investigate the effect of processing parameters on the shear stress.

Figure 9 shows the variation of shear stress distribution on the workpiece surface along the *y*-direction versus different workpiece rotational speed with the increase of working distance the MRSTP media flow velocity of 0.8 m/s. It was seen that the minimum shear stress value appeared near the low side of the workpiece. This was attributed to the combined effects between workpiece rotation and MRSTP media flow. During the numerical simulation, the flow direction of the MRSTP media was set along *x*-direction and the workpiece rotational speed was defined as counter clockwise as labelled in Fig. 9. Hence, along the *y*-axis, the linear velocity of the workpiece and the flow velocity of the MRSTP media gradually varied from the same direction to the opposite direction. This caused that the minimum shear rate in the polishing process occurred close to the point C. When the workpiece rotational speed increased, the shear stress near the D point increased. Meanwhile, the location of the minimum shear stress on the workpiece surface gradually moved upward.

Figure 10 shows the variation of shear stress distribution versus MRSTP media flow velocity of 0.8 m/s, 1.2 m/s, and 1.6 m/s with the increase of working distance at the workpiece rotational speed of 2000 rpm. As the MRSTP media flow velocity increased, the shear stress near the D point increased. The location of the minimum shear stress on the workpiece surface gradually shifted downward.

It was found that the maximum normal pressure on the workpiece surface occurred at the point A while the maximum shear stress occurred at the point D in the MRSTP as shown in Figs. 9 and 10. With the increase the workpiece rotational speed, the normal pressure on the workpiece surface decreased while the shear stress increased. It might lead to nonuniform polishing due to the upward shift of

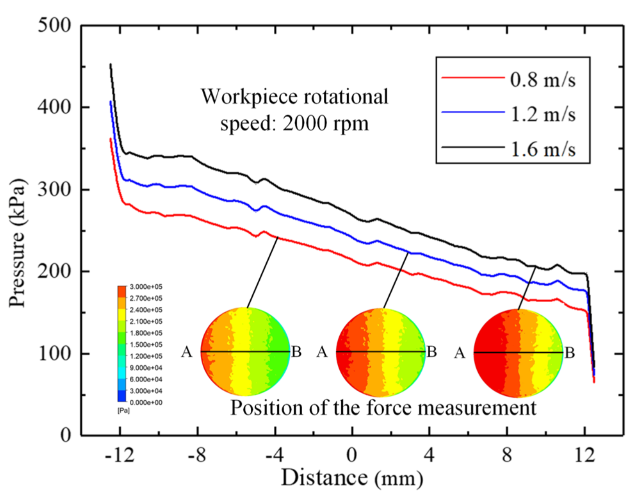

Fig. 8 Variation of normal pressure distribution versus flow velocity of MRSTP media

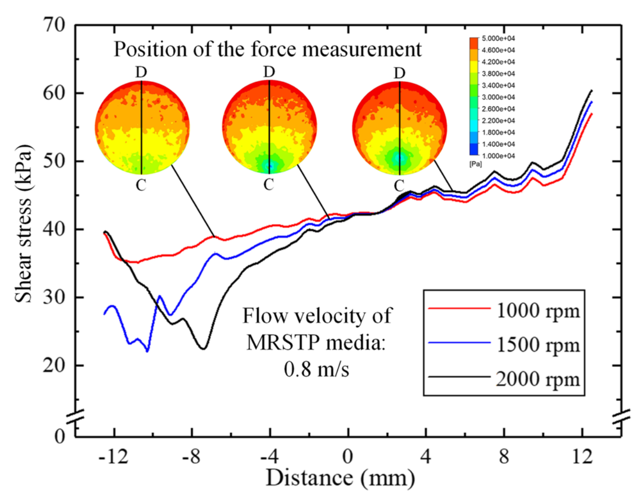

Fig. 9 Variation of shear stress versus workpiece rotational speed

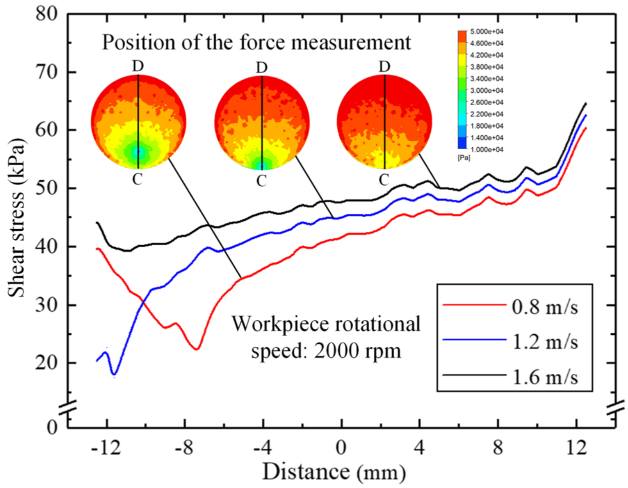

Fig. 10 Variation of shear stress versus flow velocity of MRSTP media

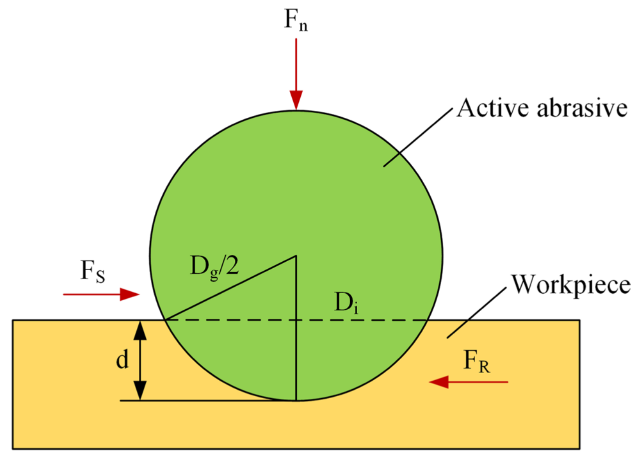

Fig. 11 Illustration of acting force of a single grain on workpiece surface

the minimum shear stress location. As the MRSTP media flow velocity increased, both the normal pressure and shear forces on the workpiece surface became large. Due to the downward shift of the minimum shear stress location, the polishing uniformity of the workpiece surface was positively affected. Hence, in the actual MRSTP process, the polishing efficiency and uniformity would be improved with low workpiece rotational speed and high the MRSTP media flow velocity.

5 Modeling of material removal rate

5.1 Forces in the MRSTP process

Figure 11 shows illustration of the acting force of a single abrasive grain on workpiece surface during MRSTP process. Under the action of the normal pressure F_n, the abrasive grain generates an indentation depth d on the workpiece surface. Because of the relative movement between the workpiece and the media fluid, the abrasive grain is subjected to the shear force F_s. When the reacting force F_R is less than the shear force F_s, the relative motion of the abrasive grain occurs to achieve the material removal on the workpiece [25, 26].

According to the Preston equation [27–29] as expressed as below.

$$MRR = k \cdot p \cdot v \tag{5}$$

where k is the Preston coefficient, p is the normal pressure applied to the workpiece surface, and v is the instantaneous relative velocity of the workpiece surface at the point of contact with the media, the material removal rate is a function of the normal pressure on the workpiece surface and the relative velocity between the workpiece and the media. The normal pressure on the workpiece surface during MRSTP consist of the three components i.e. the fluid dynamic pressure P_d, the floating force of the polishing media P_f and the magnetic pressure P_m [14]:

$$p = p_d + p_f + p_m \tag{6}$$

As both the rheological properties of the STFs and the magnetic field on the kinematic state of the MRSTP media were considered in the numerical simulation (Sect. 4. 2), the pressure in the numerical simulation was the sum of the mentioned the three different pressures viz: P_d, P_f and P_m.

According to the simulation results, the normal pressure distribution on the workpiece surface was almost unchanged along the y-axis direction while the normal pressure on the workpiece surface decreased along the x-axis direction. To simplify the calculation, the surface of the workpiece was divided into N bar areas as shown in Fig. 12.

When N is infinite, all these N regions could be considered as rectangular regions. At this point, the normal pressure in the region D_i ($i = 1, 2, 3…N$) are equal at each point, the normal pressure was defined as p_i ($i = 1, 2, 3…N$). Therefore, the total pressure on the region D_i can be calculated as:

$$p_{\mathrm{i}} = \overline{p}_i \cdot S_{Di} \tag{7}$$

$$S_{Di} = \frac{50}{N} \cdot \sqrt{25^2 - \left(25 - \frac{25}{N} i\right)^2} \tag{8}$$

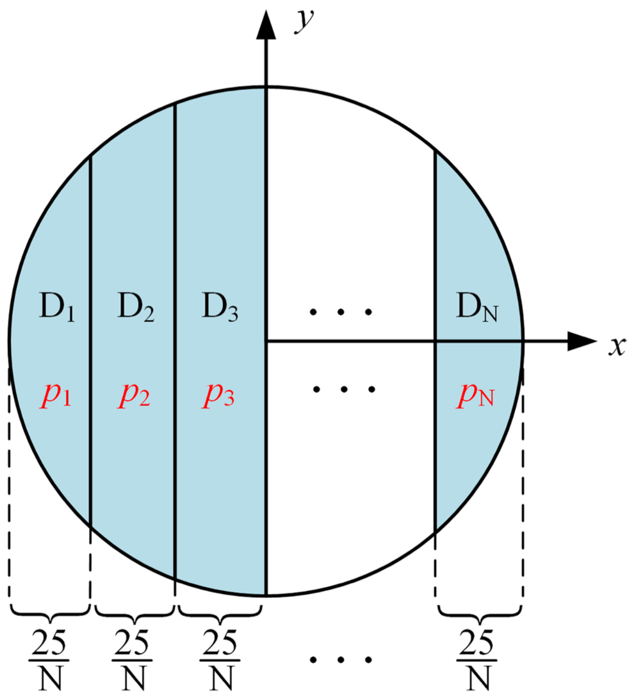

Fig. 12 Area division of the workpiece surface

where S_{Di} is the area of region D_i. Thus, when N tended to infinity, the total pressure on the workpiece surface can be expressed as:

$$p = \lim_{N\to+\infty} \sum_{i=1}^{N} p_i \tag{9}$$

Substituting Eq. (5), (6) into Eq. (7), it was yielded as:

$$p = \lim_{N\to+\infty} \sum_{i=1}^{N} \overline{p}_i \cdot \frac{1250}{N} \cdot \sqrt{\frac{i}{N}\left(2-\frac{i}{N}\right)} \tag{10}$$

5.2 Relative velocity in the MRSTP process

Figure 13 shows a simplified kinematic model of the MRSTP. O_1 is the rotation center of the spindle and O_2 is the rotation center of the rotary table. The xO_1y coordinate system is established with O_1 as the coordinate origin. ρ is the radius of the polishing bowl and ρ_0 is the eccentric distance between the spindle and the rotary table. It is assumed that the workpiece rotated around the spindle with angular velocity ω_1 and the polishing bowl rotated around the rotary table with angular velocity ω_2. The linear velocity of any point P on the surface of the workpiece is $\boldsymbol{v_1}$ about O_1 and $\boldsymbol{v_2}$ about O_2. Hence, the sum of $\boldsymbol{v}_1$ and $\boldsymbol{v}_2$ is the instantaneous relative velocity $\boldsymbol{v}$ at the point of contact between the

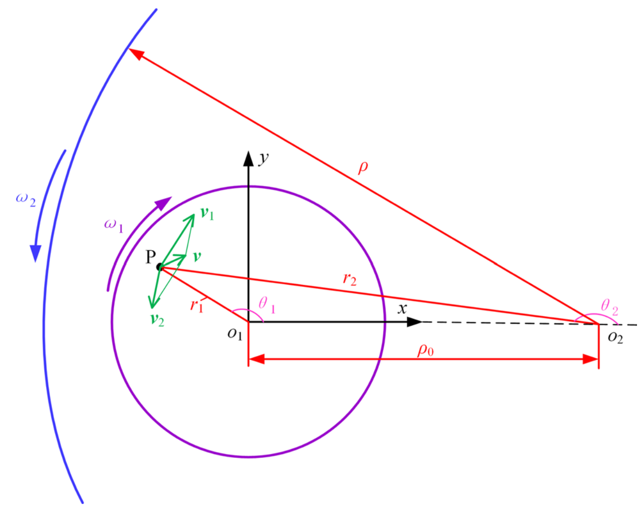

Fig. 13 A simplified kinematic model of the MRSTP

workpiece surface and the MRSTP media. The bit vectors of point P about O_1 and O_2 are defined as $\boldsymbol{r}_1$ and $\boldsymbol{r}_2$, respectively. The included angles of the line between P and O_1 and the line between P and O_2 in the positive direction of the x-axis were θ_1 and θ_2, respectively.

The relative velocity of the workpiece and MRSTP media at point P can be expressed as:

$$\vec{v} = \vec{v}_1 + \vec{v}_2 \tag{11}$$

$$\begin{cases} \vec{v}_1 = -\vec{r}_1 \cdot \omega_1 \\ \vec{v}_2 = \vec{r}_2 \cdot \omega_2 \end{cases} \tag{12}$$

The velocities $\boldsymbol{v}_1$ and $\boldsymbol{v}_2$ along the x and y axes are decomposed, respectively. Meanwhile, according to the formula for relative velocity v and the geometric relationship as shown in Fig. 13, the formulas are deduced as below.

$$v = \sqrt{v_x^2 + v_y^2} \tag{13}$$

$$r_2 = \sqrt{\left(r_1\sin\theta_1\right)^2 + \left(\rho_0 - r_1\cos\theta_1\right)^2} \tag{14}$$

$$\cos\left(\theta_1 - \theta_2\right) = \frac{r_1^2 + r_2^2 - \rho_0^2}{2r_1r_2} \tag{15}$$

The instantaneous relative velocity of the contact point between the workpiece surface and the MRSTP media is obtained as below [30]:

$$v = \sqrt{r_1^2\left(\omega_1 - \omega_2\right)^2 + \rho_0^2\omega_2^2 + 2r_1\rho_0\left(\omega_1 - \omega_2\right)\omega_2\cos\theta_1} \tag{16}$$

Fig. 14 MRSTP experimental setup

5.3 Material removal rate model in MRSTP process.

Based on the Preston equation, the theoretical material removal rate for a planar workpiece surface is expressed as:

$$MRR_t = \iint_D k \cdot p \cdot v d\sigma \tag{17}$$

Substituting Eq. (8) and Eq. (14) into Eq. (15), the Eq. (16) is yielded as below.

$$MRR_t = k \lim_{N \to +\infty} \sum_{i=1}^{N} \overline{p}_i \cdot \frac{2 \cdot 25^2}{N} \cdot \sqrt{\frac{i}{N}\left(2 - \frac{i}{N}\right)} \cdot \iint_D \sqrt{r_1^2(\omega_1 - \omega_2)^2 + \rho_0^2\omega_2^2 + 2r_1\rho_0(\omega_1 - \omega_2)\omega_2 \cos\theta_1} d\sigma \tag{18}$$

where k is the Preston coefficient, which is a constant determined by the processing conditions including magnetic field. N is the number of workpiece surface division areas. I ($i = 1, 2, 3 \ldots N$) is the serial number of the area. p_i is the pressure at any point on the area i, obtained from the simulation results. r_1 is the distance from any point P on the workpiece to the center of rotation of the spindle. ω_1 and ω_2 are the rotational speeds of the spindle and rotary table, respectively. ρ_0 is the eccentric distance between the spindle and the rotary table. θ_1 is the angle between the line connecting the point P and the center of rotation of the spindle with the positive direction of the x-axis. Equation (16) showed that the MRR is related to the MRSTP geometry configuration and process variables. The key process variables are the rotational speeds of the spindle and rotary table and working gaps.

Table 2 Experimental parameters

Items	Parameters
Spindle rotational speed (rpm)	1000, 1250, 1500, 1750, 2000
Rotational speed of rotary table (rpm)	25, 50, 75, 100, 125
Working gap (mm)	1
CIP particle size (μm)	18
SiC particle size (μm)	13
Weight ratio (CIP: SiC)	3:1
STFs concentration (wt %)	20

6 Experimental details

To verify the accuracy of the material removal model and the validity of the simulation results, a series of experiments was carried out. The experimental setup was built up on a CNC machining center (VKN640), as

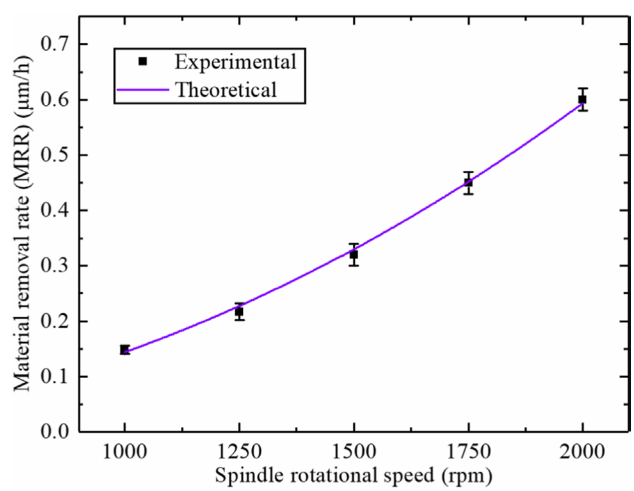

Fig. 15 Influence of spindle rotational speed on MRR

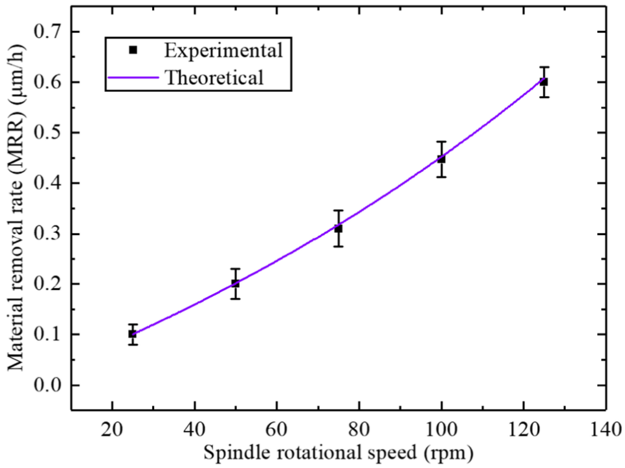

Fig. 16 Influence of rotational speeds of rotary table on MRR

shown in Fig. 14. The magnetic field generation device was installed on a vertical slipway to adjust the working gap. The vertical slipway was held to the CNC worktable by a magnetic base. The workpiece was fixed on the spindle. The polishing bowl was installed on the rotary table. The MRSTP media were contained in the polishing bowl. Magnetic-enhanced particle clusters were formed under the action of magnetic field. The workpiece relative motion was generated with the magnetic-enhanced particle cluster to achieve material removal via the rotation of the workpiece and bowl [31].

A circular Aluminum alloy 6061 with diameter of 25 mm and thickness of 5 mm was used as the workpiece. The initial (S_a) value of the workpiece surface was 337.63 nm. The working gap between the workpiece and the polishing bowl was chosen as 1.0 mm. The concentration of STF base fluid was 20 wt% in the MRSTF media. For comparison with the simulation results, the flow velocity of the MRSTP media in the simulation parameters were converted into the rotational speed of the rotary table. The detailed experimental parameters and their values are shown in Table 2.

7 Results and discussion

7.1 Verification of material removal rate model

The theoretical material removal rate (MRR_t) of MRSTP was compared with the experimental material removal rate (MRR_e). MRR_t was calculated by Eq. (16). MRR_e was calculated by Eq. (17) as below:

$$MRR_e = \frac{M_i - M_p}{S \cdot \rho \cdot t} \quad (19)$$

where, M_i was the initial mass of the workpiece, M_p was the mass of the workpiece after MRSTP, S was the area of the polished plane of the workpiece, ρ was the density of the workpiece, t was the polishing time of MRSTP.

The error Er between MRR_t and MRR_e could be calculated by Eq. (18) [32]:

$$Er = \left| \frac{MRR_t - MRR_e}{MRR_e} \right| \times 100\% \quad (20)$$

The effect of different spindle rotational speeds on MRR was investigated, as shown in Fig. 15. As the spindle rotational speed increased, the MRR increased approximately as a power function. This phenomenon was consistent with the expression of the Preston equation. As the relative velocity of the workpiece and the media increased with the increase of spindle rotational speed, the MRR became large. Although the workpiece surface pressure decreased as the spindle rotational speed increased (see Fig. 7), the reduction in normal pressure played less role in the MRR than the relative velocity.

Figure 16 shows the effects of rotational speeds of the rotary table on the MRR. It was seen that the MRR also increased with the increase of rotational speed of the rotary table. According to Eq. (15), the relative velocity of the workpiece and MRSTP media became large with the increase of rotational speeds of rotary table. Meanwhile, according to Fig. 8, the normal workpiece pressure also increased as rotational speed of the rotary table increased. This resulted in large MRR.

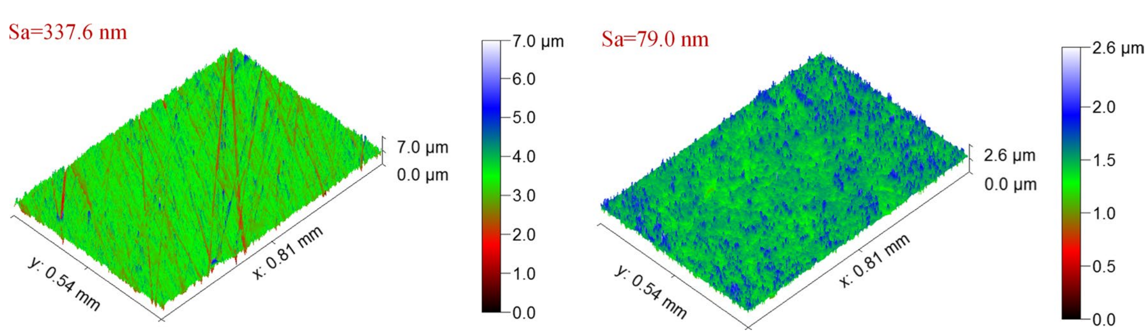

Fig. 17 3D topography of workpiece surface before and after MRSTP

According to Fig. 15 and Fig. 16, the MRR_t of the MRSTP aligned well with the MRR_e. The average error was only 4.1%. The accuracy and validity of the MRR model was verified.

7.2 Surface morphology after polishing

Figure 17 shows the 3D morphology of the workpiece (Aluminum alloy 6061) surface before and after MRSTP. It was observed that there were obvious scratches on the workpiece surface before polishing. After polishing for 1 h, the scratches on the workpiece surface were completely removed. The surface roughness (S_a) of the workpiece surface decreased from 337.6 nm to 79.0 nm, which improved by 77%. The results demonstrated that MRSTP was effective to obtain excellent polishing performance for the Aluminum alloy 6061 workpiece.

8 Conclusions

In this work, CFD method was employed to investigate the effect of polishing parameters on normal and shear stress in the MRSTP process. The MRR model of MRSTP process was established based on the CFD pressure output and the Preston equation. The accuracy and validity of the MRR model was verified. The effect of polishing parameters on the MRR was investigated. The main conclusions were drawn as follows:

(1). The CFD simulation results showed that the pressure on the workpiece surface decreased with the increase of the rotational speed of the workpiece while it increased with the increase of the flow velocity of the MRSTP media. A continuous increment in shear stress on the workpiece surface was observed with the increase of the rotation speed of the workpiece and the flow velocity of the MRSTP media.

(2). The MRR model indicated that the MRR had relation with the MRSTP geometry configuration and process variables. The key process variables were the rotational speeds of the spindle and rotary table and working gaps.

(3). The accuracy and validity of the simulated results and MRR model were verified. The average error between theoretical and experimental results was 4.1%.

(4). The workpiece surface roughness (S_a) decreased to 79.0 nm from initial 337.6 nm with 77% improvement after MRSTP. The scratches on the workpiece surface were completely removed after polishing for 1 h.

Author contributions Zhen Ma: Writing-original draft, Methodology, Experiment, Investigation, Yebing Tian: Conceptualization, Supervision, Investigation, Writing-review and editing, Project administration, Funding acquisition, Cheng Qian: Experiment, Investigation, Shadab Ahmad: Writing-review, Zenghua Fan: Writing-review, Zhiguang Sun: Experiment.

Funding This work was financially supported by the National Natural Science Foundation of China (Grant No. 51875329), Taishan Scholar Special Foundation of Shandong Province (Grant No. tsqn201812064), Shandong Provincial Natural Science Foundation, China (Grant No. ZR2023ME112, ZR2017MEE050), Shandong Provincial Key Research and Development Project, China (Grant No. 2018GGX103008), Scientific Innovation Project for Young Scientists in Shandong Provincial Universities (Grant No. 2019KJB030), and Key Research and Development Project of Zibo City (Grant No. 2019ZBXC070).

Data availability All authors confirm that all data and materials reported in this paper are available.

Code availability Not applicable.

Declarations

Ethics approval This study complies with the ethical standards set out by Springer. All authors read and approve the final manuscript.

Consent to participate Not applicable.

Consent for publication The manuscript is approved by all authors for publication.

Conflict of interest All authors declare that no conflict of interest exists.

References

1. Barman A, Das M (2018) Nano-finishing of bio-titanium alloy to generate different surface morphologies by changing magnetorheological polishing fluid compositions. Precis Eng 51:145–152. https://doi.org/10.1016/j.precisioneng.2017.08.003
2. Zhai Q, Zhai WJ, Gao B (2021) Modeling of forces and material removal rate in ultrasound assisted magnetorheological polishing (UAMP) of sapphire. Colloids Surf, A 628:127272. https://doi.org/10.1016/j.colsurfa.2021.127272
3. Luo H, Guo MJ, Yin SH, Chen FJ, Huang S, Lu AG, Guo YF (2018) An atomic-scale and high efficiency finishing method of zirconia ceramics by using magnetorheological finishing. Appl Surf Sci 444:569–577. https://doi.org/10.1016/j.apsusc.2018.03.091
4. Yamaguchi H, Srivastava A, Tan M, Hashimoto F (2014) Magnetic Abrasive Finishing of cutting tools for high-speed machining of titanium alloys. CIRP J Manuf Sci Tec 7(4):299–304. https://doi.org/10.1016/j.cirpj.2014.08.002
5. Li K, Ma RJ, Zhang M, Chen W, Li XB, Zhang DZ, Tang Q, Murr LE, Li JF, Cao HJ (2022) Hybrid post-processing effects of magnetic abrasive finishing and heat treatment on surface integrity and mechanical properties of additively manufactured Inconel 718 superalloys. J Mater Sci Technol 128:10–21. https://doi.org/10.1016/j.jmst.2022.03.026
6. Umehara N, Kirtane T, Gerlick R, Jain VK, Komanduri R (2006) A new apparatus for finishing large size/large batch silicon nitride (Si3N4) balls for hybrid bearing applications by magnetic float polishing (MFP). Int J Mach Tool Manu 46(2):151–169. https://doi.org/10.1016/j.ijmachtools.2005.04.015
7. Kumar M, Bharti RK, Dass M (2022) Study of surface finishing mechanism in a rotational-magnetorheological miniature gear profile polishing using novel flow restrictor. Wear 488–489:204120. https://doi.org/10.1016/j.wear.2021.204120

8. Wang CJ, Cheung CF, Ho LT, Yung KL, Kong LB (2020) A novel magnetic field-assisted mass polishing of freeform surfaces. J Mater Process Tech 279:116552. https://doi.org/10.1016/j.jmatprotec.2019.116552
9. Liu JB, Li XY, Zhang YF, Tian D, Ye MH, Wang C (2020) Predicting the Material Removal Rate (MRR) in surface Magnetorheological Finishing (MRF) based on the synergistic effect of pressure and shear stress. Appl Surf Sci 504:144492. https://doi.org/10.1016/j.apsusc.2019.144492
10. Sharma VK (2021) Modeling and analysis of a novel rotational magnetorheological abrasive flow finishing process. Int J Lightweight Mater Manuf 4(3):290–301. https://doi.org/10.1016/j.ijlmm.2021.02.001
11. Grover V, Singh AK (2018) Modelling of surface roughness in a new magnetorheological honing process for internal finishing of cylindrical workpieces. Int J Mech Sci 144:679–695. https://doi.org/10.1016/j.ijmecsci.2018.05.058
12. Guo YF, Yin SH, Ohmori H, Li M, Chen FJ (2022) A novel high efficiency magnetorheological polishing process excited by Halbach array magnetic field. Precis Eng 74:175–185. https://doi.org/10.1016/j.precisioneng.2021.11.011
13. Chen FJ, Yin SH, Zhu KJ, Ohmori H, Zhu YJ, Fan YF (2009) Two-dimension modelling for material removal of magneto-rheological finishing. China Mech Eng 20(14):1647–1650
14. Ming Y, Huang X, Zhou D, Li X (2022) A novel Non-Newtonian fluid polishing technique for zirconia ceramics based on the weak magnetorheological strengthening thickening effect. Ceram Int 48(5):7192–7203. https://doi.org/10.1016/j.ceramint.2021.11.280
15. Li WH, Li XH, Yang SQ, Li WD (2018) A newly developed media for magnetic abrasive finishing process: Material removal behavior and finishing performance. J Mater Process Tech 260:20–29. https://doi.org/10.1016/j.jmatprotec.2018.05.007
16. Qian C, Tian YB, Fan ZH, Sun ZG, Ma Z (2022) Investigation on rheological characteristics of magnetorheological shear thickening fluids mixed with micro CBN abrasive particles. Smart Mater Struct 31:095004. https://doi.org/10.1088/1361-665X/ac7bbd
17. Fan ZH, Tian YB, Zhou Q, Shi C (2020) Enhanced magnetic abrasive finishing of Ti-6Al-4V using shear thickening fluids additives. Precis Eng 64:300–306. https://doi.org/10.1016/j.precisioneng.2020.05.001
18. Zhou Q, Tian YB, Fan ZH, Qian C, Sun ZG (2021) Study on Preparation and Processing Characteristics of Magnetic Shear Thickening Finishing Media. Surf Technol 50(7):367–375. https://doi.org/10.16490/j.cnki.issn.1001-3660.2021.07.039
19. Sun ZG, Fan ZH, Tian YB, Prakash C, Guo J, Li L (2022) Post-processing of additively manufactured microstructures using alternating-magnetic field-assisted finishing. J Mater Res Technol 19:1922–1933. https://doi.org/10.1016/j.jmrt.2022.05.176
20. Chen FJ, Hao SM, Miao XL, Yin SH, Huang S (2018) Numerical and experimental study on low-pressure abrasive flow polishing of rectangular microgroove. Powder Technol 327:215–222. https://doi.org/10.1016/j.powtec.2017.12.062
21. Li M, Lyu BH, Yuan JL, Dong CC, Dai WT (2015) Shear-thickening polishing method. Int J Mach Tool Manu 94:88–99. https://doi.org/10.1016/j.ijmachtools.2015.04.010
22. Li M, Liu MH, Riemer O, Karpuschewski B, Tang C (2021) Origin of material removal mechanism in shear thickening-chemical polishing. Int J Mach Tool Manu 170:103800. https://doi.org/10.1016/j.ijmachtools.2021.103800
23. Li M, Karpuschewski B, Riemer O (2022) Controllable shearing chain-thickening polishing process for machining of barium borate. Int J Mach Tool Manu 37:291–301. https://doi.org/10.1016/j.cirpj.2022.02.005
24. Zhu WL, Beaucamp A (2022) Generic three-dimensional model of freeform surface polishing with non-Newtonian fluids. Int J Mach Tool Manu 172:103837. https://doi.org/10.1016/j.ijmachtools.2021.103837
25. Kumar M, Ahmad S, Das M (2021) Magnetorheological finishing of miniature gear teeth profiles using uniform flow restrictor. Mater Manuf Processes 37(4):467–482. https://doi.org/10.1080/10426914.2021.1954193
26. Prakash C, Singh S, Pramanik A, Basak A, Królczyk G, Bogdan-Chudy M, Wu YL, Zheng HY (2021) Experimental investigation into nano-finishing of β-TNTZ alloy using magnetorheological fluid magnetic abrasive finishing process for orthopedic applications. J Mater Res Technol 11:600–617. https://doi.org/10.1016/j.jmrt.2021.01.046
27. Preston FW (1927) The Theory and Design of Plate Glass Polishing Machines. J Soc Glass Technol 11:214–256
28. Zhu WL, Beaucamp A (2020) Non-Newtonian fluid based contactless sub-aperture polishing. CIRP Ann-Manuf Techn 69(1):293–296. https://doi.org/10.1016/j.cirp.2020.04.093
29. Deng JY, Zhang QX, Lu JB, Yan QS, Pan JS, Chen R (2021) Prediction of the surface roughness and material removal rate in chemical mechanical polishing of single-crystal SiC via a back-propagation neural network. Precis Eng 72:102–110. https://doi.org/10.1016/j.precisioneng.2021.04.012
30. Wang QD, Liu MC, Zhang HX (2000) Removing function of polishing pad in computer controlled optical polishing. Opt Tech 26(1):32–34. https://doi.org/10.13741/j.cnki.11-879/o4.2000.01.010
31. Tian YB, Shi C, Fan ZH, Zhou Q (2020) Experimental investigations on magnetic abrasive finishing of Ti-6Al-4V using a multiple pole-tip finishing tool. Int J Adv Manuf Tech 106:3071–3080. https://doi.org/10.1007/s00170-019-04871-z
32. Zhou DD, Huang XM, Ming Y, Li XY, Li HY, Li W (2021) Material removal characteristics of magnetic-field enhanced shear thickening polishing technology. J Mater Res Technol 15:2697–2710. https://doi.org/10.1016/j.jmrt.2021.09.092